



HAL
open science

The simulation of ELMs mitigation by pedestal coherent mode in EAST using BOUT++

Y.L. Li, T.Y. Xia, X.L. Zou, C. Zhou, X.J. Zhang, Y.R. Zhu, T.F. Tang, S.F. Mao, B. Gui, Y.Q. Huang, et al.

► To cite this version:

Y.L. Li, T.Y. Xia, X.L. Zou, C. Zhou, X.J. Zhang, et al.. The simulation of ELMs mitigation by pedestal coherent mode in EAST using BOUT++. Nuclear Fusion, 2022, 62 (6), pp.066018. 10.1088/1741-4326/ac5449 . cea-04790812

HAL Id: cea-04790812

<https://cea.hal.science/cea-04790812v1>

Submitted on 19 Nov 2024

HAL is a multi-disciplinary open access archive for the deposit and dissemination of scientific research documents, whether they are published or not. The documents may come from teaching and research institutions in France or abroad, or from public or private research centers.

L'archive ouverte pluridisciplinaire **HAL**, est destinée au dépôt et à la diffusion de documents scientifiques de niveau recherche, publiés ou non, émanant des établissements d'enseignement et de recherche français ou étrangers, des laboratoires publics ou privés.

The simulation of ELMs mitigation by pedestal coherent mode in EAST using BOUT++

Y.L. Li^{1,2}, T.Y. Xia^{2,*}, X.L. Zou³, C. Zhou¹, X.J. Zhang², Y.R. Zhu⁴, T.F. Tang⁵, S.F. Mao¹, B. Gui², Y.Q. Huang^{1,2}, G.H. Hu², M.Y. Ye^{1,*} and the EAST Team^a

¹ School of Nuclear Science and Technology, University of Science and Technology of China, Hefei, China

² Institute of Plasma Physics, Chinese Academy of Sciences, Hefei, China

³ CEA, IRFM, F-13108 Saint-Paul-lez-Durance, France

⁴ Southwestern Institute of Physics, PO Box 432, Chengdu 610041, China

⁵ College of Physics and Optoelectronic Engineering, Shenzhen University, Shenzhen 518060, China

E-mail: xiaty@ipp.ac.cn and yemy@ustc.edu.cn

Received 23 March 2021, revised 23 January 2022

Accepted for publication 10 February 2022

Published 5 April 2022



CrossMark

Abstract

A general phenomenon that the edge localized modes (ELMs) can be effectively mitigated with the enhanced coherent modes (CMs) has been observed on EAST. For this phenomenon, the experimental statistical analysis and electromagnetic (EM) simulations have been performed. There is a threshold value of the CM intensity in the experiments, which plays a key role in ELMs mitigation. Through the ELITE and conventional BOUT++ analysis, we found that when the insignificant ELM and enhanced CM co-exist, the pedestal is located in unstable P–B region and the ELM is relatively large. The simulation results only using the experimental profiles without considering other factors cannot reproduce the no significant ELM experiment. The CM enhances the edge turbulence, which can control ELMs. Therefore, the effects of CM are considered to explain the ELM mitigation. Modifying the three-field reduced model in BOUT++, an imposed perturbation is added as the CM. The simulation results indicate that: without the CM, the ELM size belongs to the relative large ELM region; after considering the CM, the ELM is mitigated and the energy loss is reduced by about 44.5%. Analysis shows that the CM enhances the three-wave nonlinear interactions in the pedestal and reduces the phase coherence time (PCT) between the pressure and potential, which lead the perturbation to tend to be ‘multiple-mode’ coupling. The competition of free energy between the multiple modes leads to the lack of obvious filament structures and the decreased energy loss. The above reveals that there is a competitive relationship between turbulence and ELMs, and the CM-enhanced turbulence can effectively reduce ELM energy loss. In addition, through the parameter scanning, there is a threshold of the amplitude A , which is consistent with the statistical results in the experiments.

Keywords: ELM mitigation, nonlinear interaction, phase coherence time (PCT), coherent mode (CM)

(Some figures may appear in colour only in the online journal)

* Authors to whom any correspondence should be addressed.

^a See Ida *et al* 2018 (<https://doi.org/10.1088/1361-6587/aa9b03>) for the EAST Team.

1. Introduction

Since the first discovery of the high-confinement regime (H-mode) in 1982 [1], ELMs have been a hot topic for the study of fusion energy. The H-mode has the characteristics of higher temperature and density at the core of the plasma, while forming an edge transport barrier at the boundary [2]. This results in the steep pressure gradients and large bootstrap currents in the pedestal, which drives the instabilities of the peeling–ballooning (P–B) mode and cause the ELMs burst [3–5]. The ELM quasi-periodic bursts generate a large amount of heat and particles pulsing out of the last closed flux surface (LCFS) and into the scrape-off layer (SOL). The impulsive heat flux can cause the erosion and damage of the plasma-facing components (PFCs), especially the divertor target plates. Therefore, understanding the physics of edge turbulence and controlling the ELMs are very important issues.

Nowadays, many effective techniques have been developed to mitigate ELMs, such as resonance magnetic perturbations (RMPs) [6, 7], low-hybrid waves (LHWs) heating [8–10], pellet injection [11], supersonic molecular beam injection (SMBI) [12] and so on. The main idea of these control methods is to produce some disturbances at the boundary of plasma, such as magnetic field, density, etc. In particular, there are two possible mechanisms of LHW ELM mitigation proposed by EAST and HL-2A. The experiment in EAST reveals that the ELM mitigation is the result of the changing edge magnetic topology, induced by helical current filaments (HCFs) in SOL due to LHWs, just like RMPs [8, 13]. In HL-2A, the ELM mitigation is mainly caused by the enhanced CM or edge turbulence, generated by LHWs inducing a reduced $E \times B$ velocity shear rate in the pedestal [10]. In fact, the both phenomena are not directly related to LHW, and the improving edge turbulence plays a key role in the ELM mitigation.

The CMs have been discovered at the boundary of plasma in tokamak devices [14]. When CM is present, it is often accompanied by the ELM mitigation and suppression. The edge turbulence can be effectively enhanced by the CM [15–20], which plays a key role in the reduction of ELMing energy loss. There are many kinds of CMs, such as the quasi-coherent mode (QCM) in C-Mod [21, 22] dominated by resistive ballooning mode (RBM) and drift-Alfvén wave (DAW), the high-frequency coherent (HFC) mode in DIII-D [23] driven by kinetic ballooning mode (KBM), the edge harmonic oscillation (EHO) in DIII-D [24] and JET [25] related to the edge pressure or pressure gradient, the weakly coherent mode (WCM) in C-Mod [26] and ASDEX Upgrade [27, 28] driven by a drift-wave instability, etc.

Recently, we found a general phenomenon in EAST experimental research: when the intensity of CM is strong enough, the ELM can be effectively mitigated. This CM is mainly the density fluctuation and driven by the pressure gradient [15]. Based on the experiment of EAST, this paper will analyze the physical mechanisms of the ELM mitigation by the CM-enhanced turbulence in EAST. The BOUT++ framework is a good tool to study the tokamak edge plasma physics, which has successfully simulated the ELM crash process [29–31]. Based on this framework, the turbulence models containing the effect

of RMP [32], HCFs [13] and pellet injection [33] have been well developed respectively, to explain the ELM mitigation. Now, we extend the three-field two-fluid turbulence model of BOUT++ by adding the CM perturbation to analyze the effects of CM on ELM mitigation.

The organization of this paper is as follows. The experiment phenomena, simulation setups and the ELM size are introduced in section 2. The physics model and the construction of the CM are described in section 3. In section 4, the impacts of the CM are simulated and analyzed. The understanding of the ELM mitigation mechanism by CM is also discussed. In section 5, we discuss the effects of the CM with different parameters, scanning the amplitude, phase and toroidal spectrum. The last section is the summary.

2. Experimental phenomena and simulation setup

2.1. The experiment and analysis

The ELM mitigation accompanied by the CMs has already been discovered in several tokamak devices. On EAST, the existence of CM inside the pedestal region is a universal phenomenon, with a wide range of plasma parameters and various auxiliary heating methods [34]. The experiment that ELMs are mitigated or even completely suppressed with the enhanced CM has already been observed in EAST, just as shown in figure 1. Shot #77741 is a H-mode discharge achieved by about 2 MW LHW and 1 MW ECRH heating. In the whole discharge process, the basic parameters are changed little, including the plasma current $I_p \sim 0.46$ MA, stored energy $W \sim 155$ kJ, poloidal beta $\beta_p \sim 1.2$, safety factor $q_{95} \sim 5.9$ and line-average density $n_e \sim 3.7 \times 10^{19} \text{ m}^{-3}$. Figure 1(d) gives a time trace of the D_α signal, which can characterize the edge radiation emission and the activity of the instabilities in the pedestal. Figure 1(e) shows the spectrum of the density fluctuations in the pedestal measured by the Doppler backscattering (DBS) [35, 36]. There is a CM with frequency about 15–20 kHz. Figure 1(f) is the time trace of the CM and turbulence intensity, which is obtained from the average of power spectral density (PSD) in different frequency ranges. It can be clearly seen that the turbulence is enhanced by the enhancement of CM. Figure 1(g) plots the evolution of ELM size and CM intensity during the ELM mitigation and suppression, respectively. The experimental ELM sizes are obtained from the magnetic perturbation signal [37–39], which can be used to estimate the energy loss during ELM crash.

The CM is enhanced obviously after about 4.1 s due to the changing heating, meanwhile the ELM is effectively suppressed. As for this CM, analysis has showed that the appearance of the CM is closely related to the pedestal electron pressure, and suggests that the mode is a kind of pressure-driven instability [15]. The CM could regulate the edge turbulence, then the ELM was mitigated or even suppressed with the CM-enhanced turbulence.

Figures 1(h)–(k) display the other two discharges, in which the plasma parameters are similar to the shot #77741. The spectrum of the CM for shot #77730 is shown in figure 1(h). Figure 1(i) represents the time evolution of the ELM size and

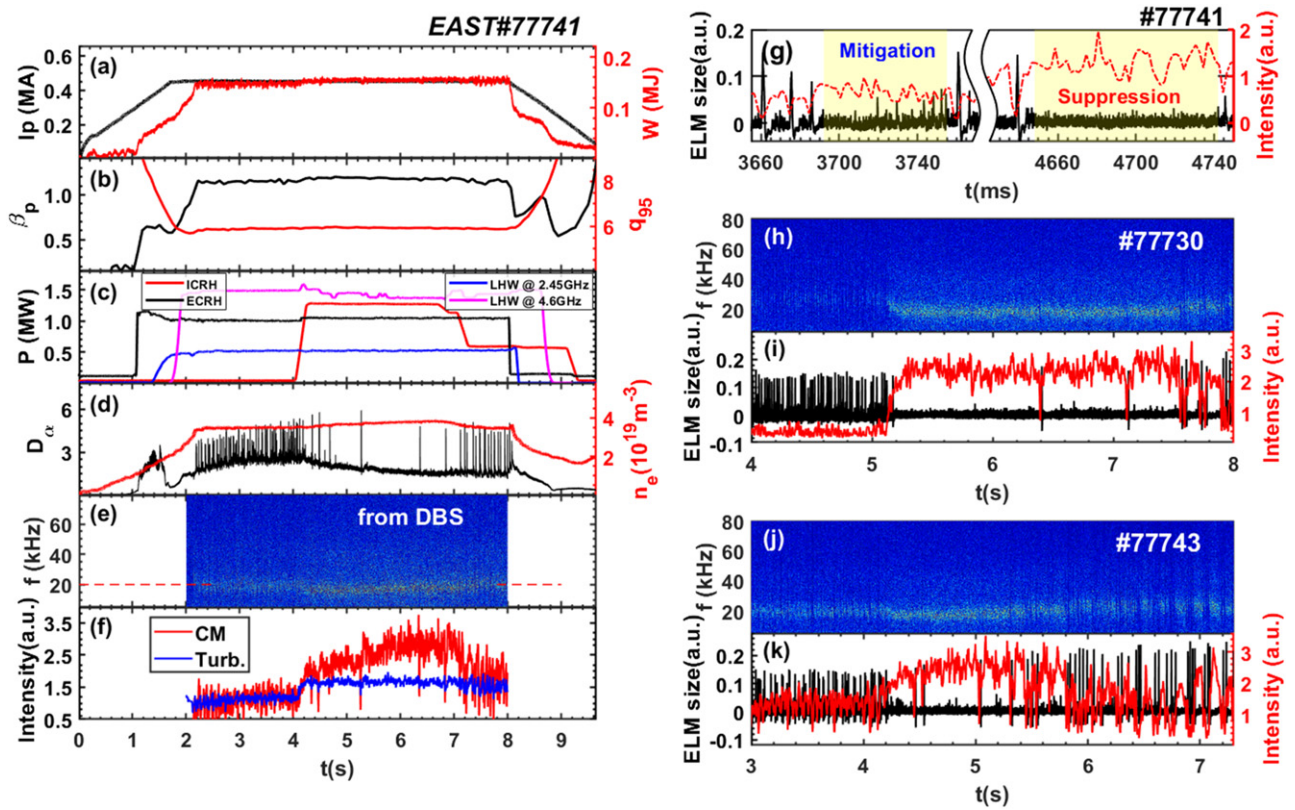


Figure 1. Time traces for the EAST H-mode discharges. Panels (a)–(g) is the parameters of shot #77741: (a) the plasma current I_p and stored energy W ; (b) the poloidal beta β_p and edge safety factor q_{95} ; (c) the auxiliary heating power; (d) the D_α signal and line-averaged density; (e) the density fluctuation spectrogram measured by DBS; (f) the intensity of the CM and the turbulence; (g) the ELM size and CM intensity during 3.66 s–3.77 s and 4.66 s–4.79 s. The panel (h) is the density fluctuation spectrogram in shot #77730, and panel (i) gives the ELM size and the CM intensity in shot #77730. (j) and (k) Are the same figures for shot #77743. Here, the ELM size is obtained from the magnetic perturbation signal.

the CM intensity. It is clearly shown that the ELM is effectively mitigated by the enhanced CM. Figures 1(j) and (k) are the same plot for the shot #77743. The strong correlation between the increase of fluctuation intensity and the ELM mitigation is observed here from all these plasma discharges.

In order to obtain a clear relationship between the ELM size and the CM intensity, the statistical analysis [16, 40] is performed in the EAST experiments. The statistical results of the discharges are shown in figure 2, and one symbol represents one single ELM. It illustrates that there is a threshold value of the CM intensity for ELM mitigation, only beyond which the ELM can be mitigated. What's more, the P–B mode pedestal stability analysis with the ELITE code [41] has been shown in figure 3. The calculation is based on the kinetic equilibrium [42] of the shot #77741 at 5.1 s, when the enhanced CM and ELM suppression co-exist. It indicates that the pedestal in the ELM suppression region with the enhanced CM is located outside the P–B boundary (near the corner). Therefore, the simulation results only considering the experimental profiles are not consistent with the insignificant ELM experiment. There must be some other key factors missed, such as the interactions between the CM and ELMs [14].

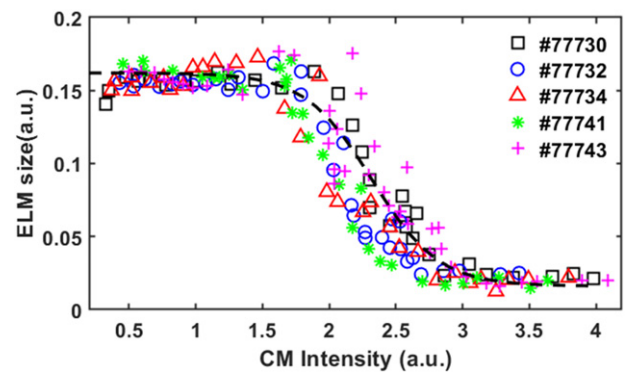


Figure 2. Statistical analysis of the EAST experiments for the relation between the ELM size and the CM intensity.

2.2. Physics model and simulation setup

In this paper, the three-field two-fluid reduced MHD model are used to simulate the P–B mode instability. This model includes the physical effects of diamagnetic drift, $E \times B$ drift, resistivity, and hyper-resistivity. A set of equations which describe the

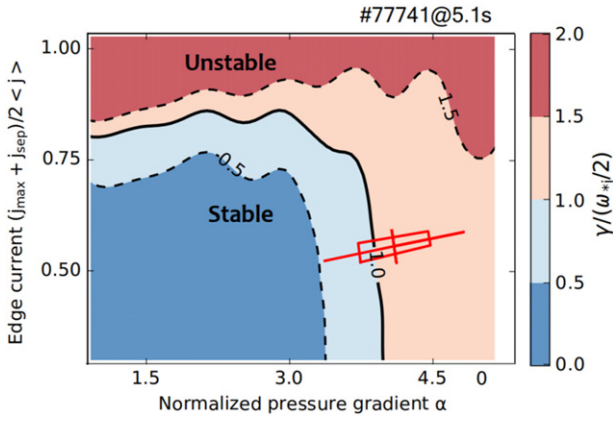


Figure 3. Pedestal PBM stability diagram calculated with the ELITE code. The color bar shows the PBM growth rate γ , normalized to half of the ion diamagnetic drift frequency, $\omega_{*i}/2$.

evolution of the perturbed variables, vorticity $\tilde{\omega}$, pressure \tilde{p} , and parallel magnetic vector potential \tilde{A}_{\parallel} , are written as [29]

$$\frac{\partial \tilde{\omega}}{\partial t} + v_E \cdot \nabla \tilde{\omega} = B \nabla_{\parallel} J_{\parallel} + 2 \vec{b}_0 \times \kappa_0 \cdot \nabla \tilde{p} \quad (1)$$

$$\frac{\partial \tilde{p}}{\partial t} + v_E \cdot \nabla P = 0 \quad (2)$$

$$\frac{\partial \tilde{A}_{\parallel}}{\partial t} = -\nabla_{\parallel} \Phi + \frac{\eta}{\mu_0} \nabla_{\perp}^2 \tilde{A}_{\parallel} - \frac{\eta_H}{\mu_0} \nabla_{\perp}^4 \tilde{A}_{\parallel} \quad (3)$$

$$\tilde{\omega} = \frac{n_0 m_i}{B} \left(\nabla_{\perp}^2 \tilde{\phi} + \frac{1}{n_0 Z_i e} \nabla_{\perp}^2 \tilde{p}_i + \frac{\nabla n_0}{n_0} \cdot \nabla \tilde{\phi} \right) \quad (4)$$

$$J_{\parallel} = J_{\parallel 0} - \frac{1}{\mu_0} \nabla_{\perp}^2 \tilde{A}_{\parallel}, \quad v_E = \frac{1}{B_0} (b_0 \times \nabla_{\perp} \Phi). \quad (5)$$

Where Φ is the electro-static potential, $\Phi = \tilde{\phi} + \Phi_0$, and $P = \tilde{p} + P_0$. $\nabla_{\parallel} F = B \partial_{\parallel} (F/B)$ for any F , $\partial_{\parallel} = \partial_{\parallel}^0 + \tilde{b} \cdot \nabla$, $\partial_{\parallel}^0 = \mathbf{b}_0 \cdot \nabla$, $\tilde{b} = \tilde{B}/B = \partial_{\parallel} \tilde{A}_{\parallel} \times b_0/B$. F_0 represents the zero order equilibrium quantity and \tilde{F} represents the perturbation. $k_0 = \mathbf{b}_0 \cdot \nabla \mathbf{b}_0$ is the curvature vector. In the equation (4), the second term on the right side represents the ion diamagnetic effect, which embodies the ‘two-fluid’. A field-aligned flux coordinate system (x, y, z) [43] is adopted in our simulation, which is derived from the orthogonal toroidal coordinate system (ψ, θ, ζ) . The relationship between the two coordinate systems is in equation (6). Here $\nu(\psi, \theta) = \mathbf{B} \cdot \nabla \zeta / \mathbf{B} \cdot \nabla \theta = B_{\zeta} h_{\theta} / B_{\theta} R$ is the local field-line pitch, and $h_{\theta} = 1/|\nabla \theta|$ is the scale factor for θ .

$$\begin{cases} x = \psi - \psi_0, \\ y = \theta, \\ z = \zeta - \int_{\theta_0}^{\theta} \nu(\psi, \theta) d\theta. \end{cases} \quad (6)$$

In order to investigate the effects of CM on the ELM mitigation, we also choose the kinetic equilibrium of the EAST H-mode discharge #77741 at 5.1 s to analyze. This discharge is the upper single null divertor configuration as shown in

figure 4. The area between the two black curves in figure 4(a) is the simulation domain with both pedestal and SOL regions, which ranges from the normalized poloidal flux $\psi = 0.8$ to $\psi = 1.05$. The spatial resolution of the mesh is $(N_x, N_y, N_z) = (260, 64, 64)$. The red curve is the last closed flux surface (LCFS), and the magenta line is the vacuum vessel of EAST device. Figures 4(b)–(d) give the initial equilibrium profiles $(P_0, n_0, T_{i0}, T_{e0})$ used in the simulation. No impurities are considered and the quasi-neutral condition is used, i.e. $n_{i0} = n_{e0}$. Boundary conditions are $\tilde{\omega} = 0$, $\nabla_{\perp}^2 \tilde{A}_{\parallel} = 0$, $\partial \tilde{p} / \partial \psi = 0$ and $\partial \tilde{\phi} / \partial \psi = 0$ on inner and outer boundaries, and there are no additional sources in the whole simulation process. To improve the efficiency of the calculation, only 1/5th of the torus is simulated [43]. In theory, the simulation results will not change fundamentally if the simulation domain changes, such as using 1/2th or 1/3th of the torus. Resistivity, hyper-resistivity, and parallel ion viscosity are chosen to be $S = \mu_0 R_0 V_A / \eta = 10^8$, $S_H = \mu_0 R_0^3 V_A / \eta_H = 10^{14}$, and $\mu_{\parallel i} = 0.1 \omega_A R^2$ for the typical pedestal plasmas [29, 30, 44]. As for the equilibrium electric field, the flow balance condition is used, $E_{r0} = \nabla P_{i0} / (n_0 Z_i e)$ [29, 30, 45], with ion pressure $P_{i0} = P_0/2$.

2.3. Energy loss and parameter selection of the simulation

Based on the physics model and the simulation setups mentioned in the previous section, a series of simulation results are presented. Figure 5(a) shows the dependence of the linear growth rate on the toroidal mode number, including the ideal P–B mode and diamagnetic drift. The positive growth rate indicates that the pedestal is unstable, which is the same as the result of the ELITE analysis in figure 3. The time evolution of the perturbed pressure and ELM size of the nonlinear simulation are plotted in figure 5(b). The perturbed pressure is obtained at the peak pressure gradient region of the outer mid-plane. The ELM size is the ratio of the ELM energy loss to the pedestal stored energy [29, 44], according to dimensions of integral, defined as $\Delta_{\text{ELM}}^{\text{1D}}(t) = \Delta W_{\text{ped}}^{\text{1D}} / W_{\text{ped}}^{\text{1D}} = \int_{R_{\text{in}}}^{R_{\text{out}}} (P_0 - P(t)_{\xi}) dR / \int_{R_{\text{in}}}^{R_{\text{out}}} P_0 dR$ and $\Delta_{\text{ELM}}^{\text{3D}}(t) = \Delta W_{\text{ped}}^{\text{3D}} / W_{\text{ped}}^{\text{3D}} = \int_{R_{\text{in}}}^{R_{\text{out}}} dR \oint J d\theta d\zeta (P_0 - P(t)_{\xi}) / (P_{\text{ped}} V_{\text{plasma}})$, respectively. Where, $\Delta_{\text{ELM}}^{\text{1D}}$ is the radial one-dimensional integral result at the outer mid-plane and $\Delta_{\text{ELM}}^{\text{3D}}$ is the three-dimensional full-space integral result. The whole ELM crash process can be divided into three stages [44] from the trace of ELM size: (1) the linear growing phase of the P–B mode; (2) the ELM bursting process and a buildup as a turbulence transport process; (3) the nonlinear saturation phase. The ELM size eventually reaches about $\Delta_{\text{ELM}}^{\text{1D}} \sim 2.88\%$ in figure 5(b), which belongs to the relative large ELM region. This result is inconsistent with the experiment. In addition, the scanning results of the resistivity, hyper-resistivity, and parallel ion viscosity are shown in figure 6. Here, a dimensionless hyper-Lundquist parameter is defined as $\alpha_H = S/S_H = \eta_H / (R_0^2 \eta)$, which can characterize the hyper-resistivity. Due to the insensitivity of the ELM size to the resistivity in today’s modestly sized tokamaks and ITER [30], the values of these parameters are all selected in the insensitive regions for our simulations (the vertical dotted lines in figure 6). Using this set of typical plasma pedestal parameters, the CM-induced ELM mitigation

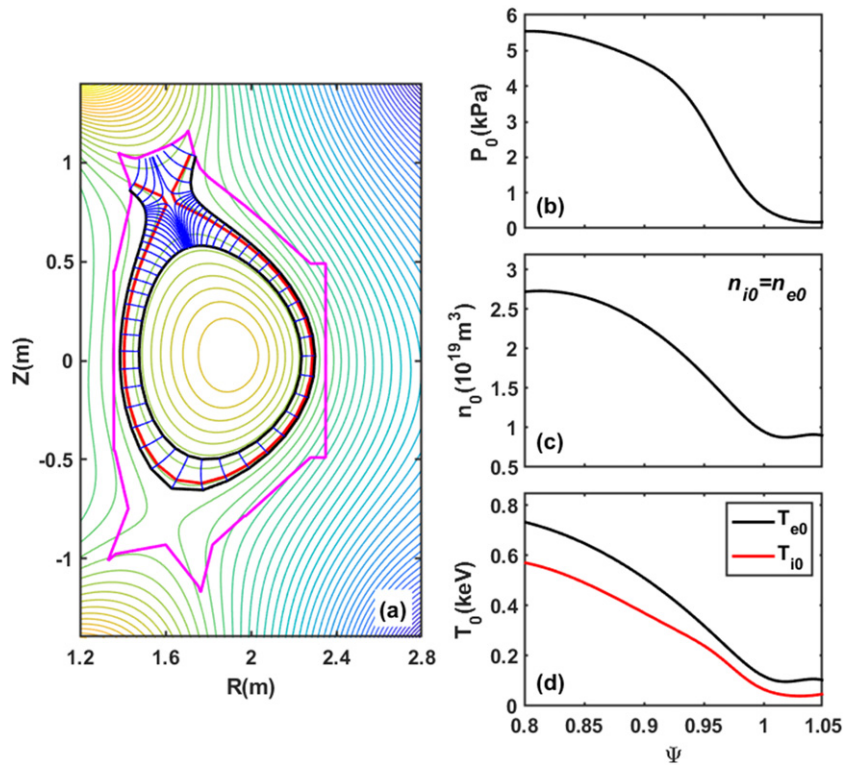


Figure 4. (a) EAST geometry and simulation domain: the red curve is the last closed flux surface, the black curves are the inner and outer boundaries, the 64 poloidal blue curves represent the simulation grids, and the magenta curve is the vacuum vessel. (b) The pressure profile. (c) The density profile ($n_{i0} = n_{e0}$). (d) The electron temperature and ion temperature.

is insensitive to these parameters. This suggests that the inconsistency with the experiment is not the problem of parameter values. Therefore, we include the effect of the CM in the expectation that the ELM can be effectively mitigated.

2.4. The spectrum of the CM

CMs have been found in many experiments on EAST and are often accompanied by the ELM mitigation [16, 46, 47]. It is believed that CMs can regulate the edge particle transport [10, 16, 20], which play a role in the pedestal dynamics. The frequency spectrogram of the pressure fluctuation from the nonlinear simulation [31, 48] is shown in figure 7, which clearly shows a characteristic of the CM. The peak of the black solid curve between the two black dashed lines is the CM with the frequency about 14–22 kHz and the center frequency is 18 kHz. The frequency of the CM is in good agreement with the experiments in figure 1. The red dashed curve only represents the spectrum of the background broadband turbulence, which is obtained by filtering out the CM frequency [49, 50]. It is important to point out that this CM is generated by the profile auto-evolution (i.e. after the ELM crash).

3. Construction of the CM physical model

In general, the boundary plasma turbulence and transport determine the edge energy loss. In section 2.3, the ELM size is not consistent with the experiment. Therefore, the impact of the CM needs to be considered and analyzed. In this section,

the modeled CM is added into the three-field two-fluid module of BOUT++.

3.1. Physics model

To account for the effect of the CM, the three-field two-fluid model is modified within the assumption that the density fluctuations is dominant in this CM. Here the perturbation of CM is artificially constructed, not automatically generated as in section 2.3, aiming to interact with the ELM. The form of the equations (1), (2) and (4) changed by the CM is written as

$$\frac{\partial \tilde{\omega}}{\partial t} + v_E \cdot \nabla \tilde{\omega} = B_0 \nabla_{\parallel} J_{\parallel} + 2\tilde{b}_0 \times \kappa_0 \cdot \nabla (\tilde{p} + \tilde{P}_{\text{CM}}), \quad (7)$$

$$\frac{\partial \tilde{p}}{\partial t} + v_E \cdot \nabla P + v_E \cdot \nabla \tilde{P}_{\text{CM}} = 0, \quad (8)$$

$$\tilde{\omega} = \frac{n_0 M_i}{B_0} \left[\nabla_{\perp}^2 \tilde{\phi} + \frac{1}{n_0 Z_i e} \nabla_{\perp}^2 (\tilde{p}_i + \tilde{P}_{\text{CM}}) + \frac{\nabla n_0}{n_0} \cdot \nabla \tilde{\phi} \right]. \quad (9)$$

In order to consider the CM effect, the additional terms with respect to the quantity \tilde{p}_{CM} are introduced in the evolution equations of vorticity $\tilde{\omega}$, pressure \tilde{p} as the source and convection terms, respectively. The \tilde{p}_{CM} represents the pressure perturbation of the CM, which can effectively affect the pedestal dynamics. The detailed construction process of \tilde{p}_{CM} will be described in section 3.2. It is worth clarifying that the main reason for this modification is that the boundary instability of EAST is mainly measured from density fluctuations, which is presented as pressure in our model.

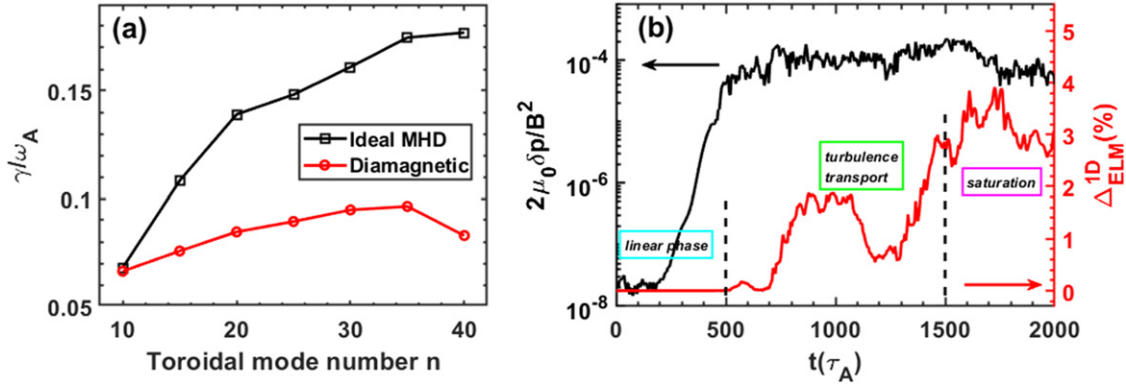


Figure 5. (a) Linear growth rate versus toroidal mode spectrum: the ideal MHD model in black square, and the diamagnetic stabilization model in red circle; (b) the perturbed pressure and ELM size evolution during the simulation. The growth rates are normalized to the Alfvén frequency $\omega_A = 2.28 \times 10^6 \text{ s}^{-1}$.

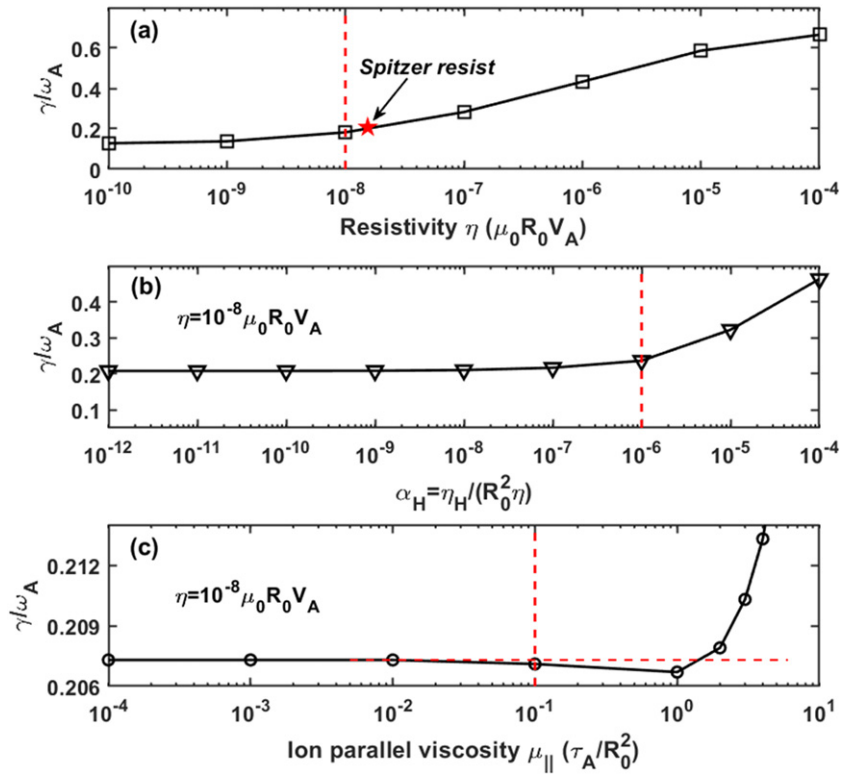


Figure 6. The growth rate of the $n = 20$ eigenmode versus various parameters with the resistivity effect: (a) the resistivity η (the red star is the spitzer resist), (b) the dimensionless hyper-Lundquist parameter α_H with $\eta = 10^{-8} \mu_0 R_0 V_A$, (c) the ion parallel viscosity $\mu_{||}$ with $\eta = 10^{-8} \mu_0 R_0 V_A$. In all the simulations, $\eta = 10^{-8} \mu_0 R_0 V_A$, $\alpha_H = 10^{-6}$ and $\mu_{||} = 0.1$ (the vertical dotted lines).

3.2. Construction of \tilde{P}_{CM}

In the experiment, it is found that the CM improves the edge turbulence, then the ELM is mitigated by the CM-enhanced turbulence [10, 15]. Therefore, the impacts of the CM are necessary to be discussed. First, in the case of section 2.3, the evolution of the simulated electrostatic potential perturbation $e\delta\phi/T_{e0}$ and magnetic fluctuation b_1/b_0 near the peak pressure gradient at the outer mid-plane are given in figure 8. The electrostatic potential perturbation is more than four orders of magnitude larger than the magnetic fluctuation, and the

average value in the nonlinear saturation phase are about: $e\delta\phi/T_{e0} = 0.356$ and $b_1/b_0 = 1.4 \times 10^{-5}$. Since $\delta n \sim \delta\phi$ [51], the disturbance is mainly density fluctuation, which meets the assumption of the physical model in section 3.1. Therefore, we assume a finite-amplitude pressure fluctuation as the perturbation of the CM (\tilde{p}_{CM}). According to the measurements by the reflectometry, the \tilde{p}_{CM} is $\sim 10^{-2} P_0$ [15]. Here the finite-amplitude pressure means that it is large enough in the linear growing phase, but small enough not to dominant the nonlinear evolution phase.

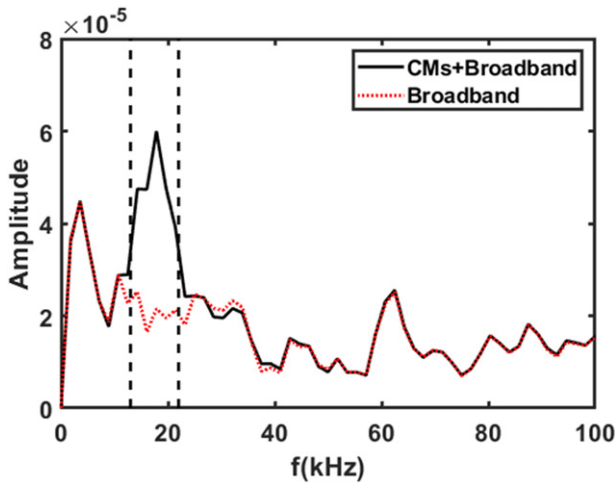


Figure 7. The frequency spectra of the pressure fluctuation from the nonlinear phase: the black solid curve is the spectra including both the CM and the background broadband turbulence, and the red dashed curve is only the spectra of broadband turbulence, while the CM frequency is filtered.

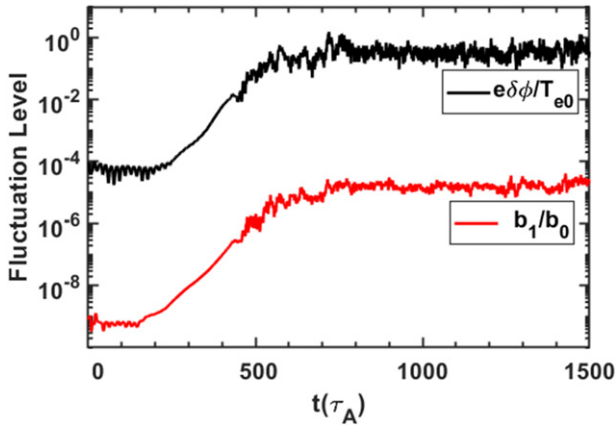


Figure 8. The comparison of the normalized electrostatic fluctuation $e\delta\phi/T_{e0}$ and magnetic fluctuation b_1/b_0 .

Figure 9 illustrates the perturbation characteristics of the case in section 2.3 during the nonlinear saturation phase. The panel (a) shows the normalized amplitude of the pressure fluctuations \bar{P}_{kz} vs the toroidal mode number, and panel (b) gives the phase spectrum over a time period, which is random for the toroidal mode n , here written as $\theta = \Theta(n)$. These spectrums cannot be measured in the experiment and will be used in the construction of the CM. In figure 9(a), the spectrum \bar{P}_{kz} which has a dominant mode of $n = 10$ (black open circle), is obtained from the CM in section 2.3. This spectrum is used to construct CM in section 4, to ensure that the ELM and CM have a strong enough interaction. While the spectrums of dominant mode $n = 20$ (red triangle) and broadband (blue square) are artificially constructed for the parametric scans in the section 5. What's more, the zonal background of the CM is partially filtered out, i.e. $\bar{P}_{kz}(n=0) = 0$, in order to keep the initial input P_0 consistent with the kinetic equilibrium and not affect the stability of the P–B modes. Notice that this constructed \tilde{p}_{CM} is a 3D

pressure perturbation, which already contains the information of the CM.

In EAST, the characteristics of CM in the experiment have been studied in reference [16]. The poloidal asymmetry of the local poloidal wavenumber for the CM has been observed and has been explained by assuming that the mode is flute-like, i.e. $k_{||} \sim 0$ [16]. Therefore, the distribution of CM parallel to the magnetic field is expressed by Gaussian function in the simulation [19, 51]. In the experiment, the toroidal mode number of the CM has been estimated to be $n = 12\text{--}17$ based on the flute-like assumption, correspondingly, $n = 10$ in the simulation of section 2.3 (shown in figure 9(a)). In addition, the poloidal distribution of the CM density fluctuation amplitude presents a ballooning-like structure in the experiment [16].

According to the characteristics of the CM measured in the experiments, the construction of \tilde{p}_{CM} is as follows:

$$\tilde{p}_{CM}(x, y, z, A) = Af(z) \cdot e^{-\frac{(x-b_1)^2}{2\sigma_x^2} - \frac{(y-b_2)^2}{2\sigma_y^2}}, \quad (10)$$

where A is the amplitude, defined as $A = |\tilde{p}_{CM}/P_0|_{\max}$. The radial and poloidal distributions of CM are described by the Gaussian function with the parameters $b_1 = 0.5$, $b_2 = 0.39$, $\sigma_x = 0.6$ and $\sigma_y = 0.1$, which can ensure the CM is mainly distributed near the outer mid-plane and covers the pedestal. As for the toroidal profile $f(z)$, it is related to the toroidal mode number n and the phase θ [16, 51], which can be obtained by the following equation:

$$f(z) = [F(n, \theta)]_{\text{IFT}}. \quad (11)$$

Where the symbol $[]_{\text{IFT}}$ means the calculation of the inverse Fourier transform (IFT). The seed perturbation $F(n, \theta)$ is defined as $F(n, \theta) = \bar{P}_{kz}(n)e^{-i\theta}$, here is $\bar{P}_{kz}(n)$ the normalized pressure fluctuation spectrum and θ can be set to $\theta = \Theta(n)$, just as shown in figure 9. Ultimately, the expression for \tilde{p}_{CM} can be written as

$$\tilde{p}_{CM}(x, y, z, A) = A \cdot e^{-\frac{(x-b_1)^2}{2\sigma_x^2} - \frac{(y-b_2)^2}{2\sigma_y^2}} [\bar{P}_{kz}(n) e^{-i\theta}]_{\text{IFT}}. \quad (12)$$

In this equation, $\tilde{p}_{CM}(x, y, z, A)$ depends on the variables $\bar{P}_{kz}(n)$, θ and A . The impact of the CM is considered by adding a source of the finite-amplitude pressure fluctuation, just as shown in equations (7) and (8). Figure 10 gives an example of the \tilde{p}_{CM} structure constructed from the equation (12). Figure 10(a) is the toroidal slice of the \tilde{p}_{CM} fluctuation, and the toroidal profile in figure 10(c) is obtained from the position of the peak pressure gradient. Figure 10(b) is the poloidal slice, and the fluctuation mainly locates at the low field side, just like the ballooning structure shown in the experiment [16]. The radial profile at the outer mid-plane is shown in figure 10(d).

4. Analysis for the impact of CM

In this section, the simulation results with the effects of CM are presented and analyzed. In the simulation, the distribution of CM (\tilde{p}_{CM}) is constructed using the equation (12), and the specific parameters are as follows: (1) set $\bar{P}_{kz}(n)$ to the spectrum with the dominant mode $n = 10$ in figure 9(a); (2) set

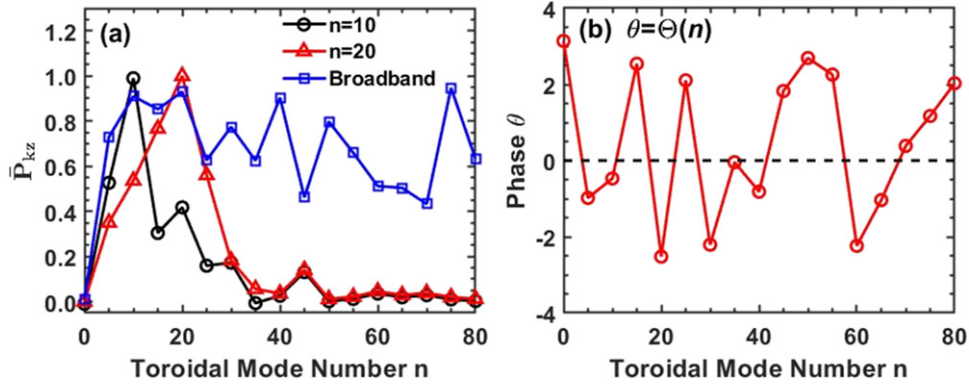


Figure 9. (a) The normalized pressure fluctuation \bar{P}_{kz} vs toroidal mode number spectra; (b) the turbulent phase θ vs toroidal mode number. Both of the spectrums are used to construct the CM.

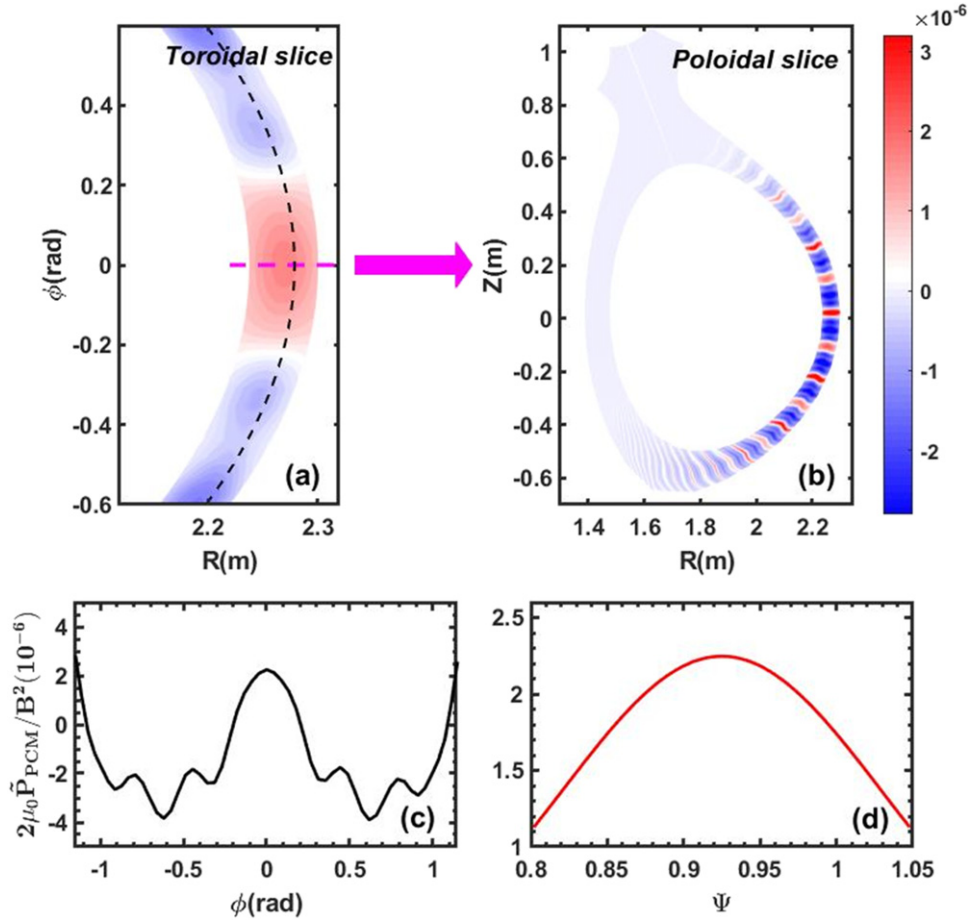


Figure 10. The structure of \tilde{p}_{CM} : (a) toroidal slice of the fluctuation of the pressure (the dashed black line is the location of the peak pressure gradient); (b) poloidal slice of the fluctuation; (c) the toroidal profile at the peak pressure gradient; and (d) the radial profile at outer mid-plane.

the turbulent phase $\theta = \Theta(n)$ as shown in figure 9(b); and (3) the amplitude is $A = 10^{-2}$. Figure 11 shows the evolution of the ELM size Δ_{ELM}^{1D} with (w/) and without (w/o) the CM, and the ELM size Δ_{ELM}^{3D} is plotted in the inset. It can be seen that Δ_{ELM}^{1D} is already saturated, but Δ_{ELM}^{3D} is not. This is mainly because the poloidal expansion of the perturbation is very slow, and hard to get saturation. Fortunately, in the experiments, the energy loss is usually calculated by radially integrating the pressure profile at the outer mid-plane with

ballooning characteristics [30], i.e. Δ_{ELM}^{1D} . In the simulation, most of the energy loss also occurs at the outer mid-plane due to the mainly ballooning-like instability. Meanwhile, the collapsed profiles will not get recovered as there is no additional source in the simulation [44]. Therefore, the saturated Δ_{ELM}^{1D} can fully represent the total energy loss of the simulation. At $t = 2000\tau_A$, the ELM size w/o CM reaches about 2.88%, and that w/ CM is about 1.60%. The ELM size is reduced by approximately 44.5% after considering the CM. In addition,

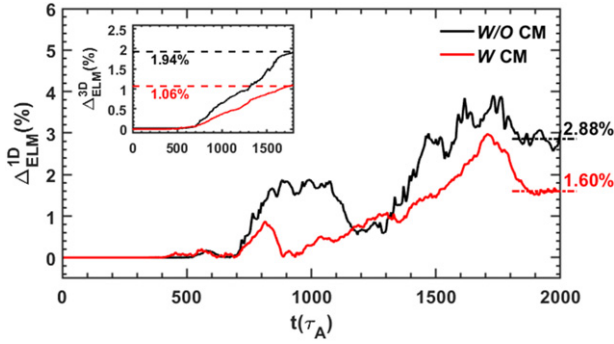


Figure 11. The time evolution of ELM size with and without the CM.

scanning the resistivity and hyper-resistivity in the effective range, the result of CM-induced ELM mitigation can also be achieved, not only under the parameters of section 2.3.

The impact of CM is analyzed by covering the following aspects: (1) the mode structure and spectrum during the nonlinear phase; (2) the nonlinear wave–wave interactions; and (3) the phase coherence time (PCT).

4.1. The mode structure and mode spectrum

Figure 12 illustrates the comparison of the distribution of pressure fluctuations w/ and w/o the CM. The radial distribution of the RMS perturbed pressures at the outer mid-plane during the later nonlinear phase 1400–1600 τ_A are shown in figure 12(a). The peak of the both RMS pressure fluctuations is near the $\psi = 0.95$, which is the same position of the peak pressure gradient. After considering the CM, the amplitude of the fluctuation is about half of that without CM. Figure 12(b) gives the time evolution of the RMS pressure fluctuations at the peak pressure gradient region of the outer mid-plane. The fluctuation w/ \tilde{p}_{CM} is smaller, which implies that the ELM is mitigated by the CM. It is worth noting that the case w/ CM enters the nonlinear phase more quickly than the case w/o CM (shown at the position of the black and red dashed lines). This is because the initial perturbation is larger due to the CM, and the amplitude of the fluctuation triggering the ELM crash can be reached earlier.

The time evolution of pressure perturbations in the cases w/ and w/o CM are shown in figure 13. The radial pressure profiles at the outer mid-plane at several time slices are displayed in the figures 13(a) and (b). In the both cases, the profile gradually collapses inward and the radial expansion of ELM occurs. However, it is clearly seen that the profile collapses only to $\psi \sim 0.88$ after considering the CM, which is shallower than the case w/o CM. Figures 13(c) and (d) show the nonlinear evolution of the different modes of pressure fluctuations for the two cases. The linear growth phase (the blue shadow) w/o \tilde{p}_{CM} is about $t = 240\text{--}480\tau_A$, and w/ \tilde{p}_{CM} is $t = 250\text{--}450\tau_A$. The linear phase w/ CM is shorter, which is due to the larger initial perturbation and the smaller saturation amplitude. During 850–1100 τ_A (the yellow shadow), the average amplitude of $n = 0$ mode is about 2.53×10^{-4} without CM and 8.65×10^{-5} with CM. There is a larger zonal component in the

case w/o CM, which represents a larger energy loss. The nonlinear mode spectrum evolution for different cases are shown in figures 13(e) and (f). We have chosen a time period of 160–800 τ_A , including the linear and early nonlinear phases. It is clearly shown that the \tilde{p}_{CM} terms shift the mode spectrum of the linear phase, but have little effect on the nonlinear phase. This is in accordance with the assumption in section 3.2 about the finite-amplitude pressure. In the case w/o CM, there is a dominant mode $n = 20$ to trigger the ELM. However, there are two clear modes ($n = 15, 20$) in the linear growing phase (magenta dashed box) for the case w/ CM, and both modes have the similar amplitude, ultimately resulting in the mitigation of ELM.

4.2. The bi-spectral analysis for wave–wave interaction

Bi-spectral analysis is a very useful signal processing technique for showing the nonlinear three-wave interactions among the fluctuating quantities [52–54]. Here it is applied to determine the degree of the nonlinear mode coupling between the ELM and the CM. The method is described as follows. The bi-spectrum \hat{B}_{XYZ} and the squared bi-coherence \hat{b}_{XYZ}^2 of the signals $x(\zeta)$, $y(\zeta)$ and $z(\zeta)$ are given by [54]

$$\hat{B}_{XYZ}(n_1, n_2) = X(n_1)Y(n_2)Z^*(n_1 + n_2). \quad (13)$$

$$\hat{b}_{XYZ}^2(n_1, n_2) = \frac{|\hat{B}_{XYZ}(n_1, n_2)|^2}{|X(n_1)Y(n_2)|^2|Z(n_1 + n_2)|^2}, \quad (14)$$

where $X(n)$, $Y(n)$ and $Z(n)$ are the space Fourier transform of $x(\zeta)$, $y(\zeta)$ and $z(\zeta)$ in the toroidal direction, respectively. $Z^*(n)$ is the conjugate of $Z(n)$, and n is the toroidal mode number. Here the auto-bispectrum is calculated, i.e. $X(n) = Y(n) = Z(n)$. The angle bracket indicates the ensemble average, which is obtained from the simulated data at different times and locations. In this definition, the bi-spectrum measures the degree of the nonlinear phase coherence among three waves of mode numbers n_1 , n_2 and n . The squared bi-coherence quantifies the power fraction at the mode $n = n_1 + n_2$ due to the three-wave coupling, revealing variations in the degree of the nonlinear interactions among the three fluctuations, not related to the amplitude of the mode.

Figure 14 shows the contour plots of squared auto-bicoherence of the pressure fluctuations ($\hat{b}_{p_n p_n p_n}^2(n_1, n_2)$) during 1000–1500 τ_A for the cases w/ and w/o CM, respectively. It can be seen that the bi-coherence values with the modes $(n_1, n_2) = (5, 5)$ and $(10, -5)$ are larger in figure 14(a), which implies that the significant level of the nonlinear interactions is concentrated at these modes in the case w/o CM. However, in the case w/ CM, there are some medium- n modes, such as $(n_1, n_2) = (15, -10)$, $(25, -15)$, $(25, -10)$, $(10, 10)$ and so on, coupled to the lower n modes, such as $n = 5, 10, 15$ and 20 as shown in figure 14(b). By comparison with figure 14(a), the red region is larger and the color is darker in figure 14(b), which indicates that there are more modes coupled and stronger nonlinear interactions in the case

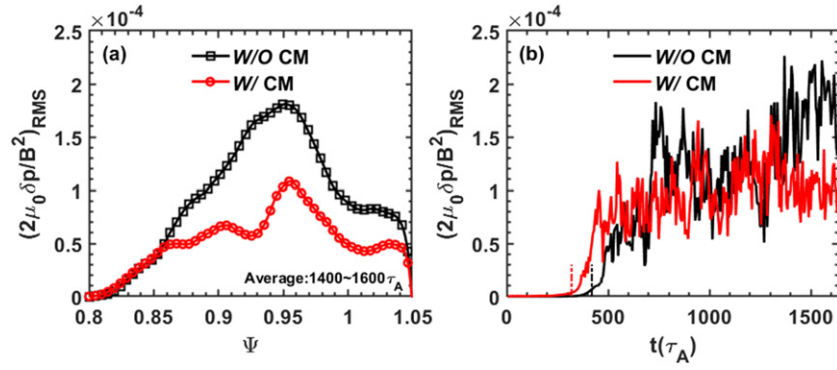


Figure 12. The results from simulated fluctuations: (a) the radial distribution of the root mean squared (RMS) perturbed pressure w/ and w/o the CM at outer mid-plane in the time average of $t = 1400\text{--}1600\tau_A$; (b) the time evolution of the RMS perturbed pressure for the same cases.

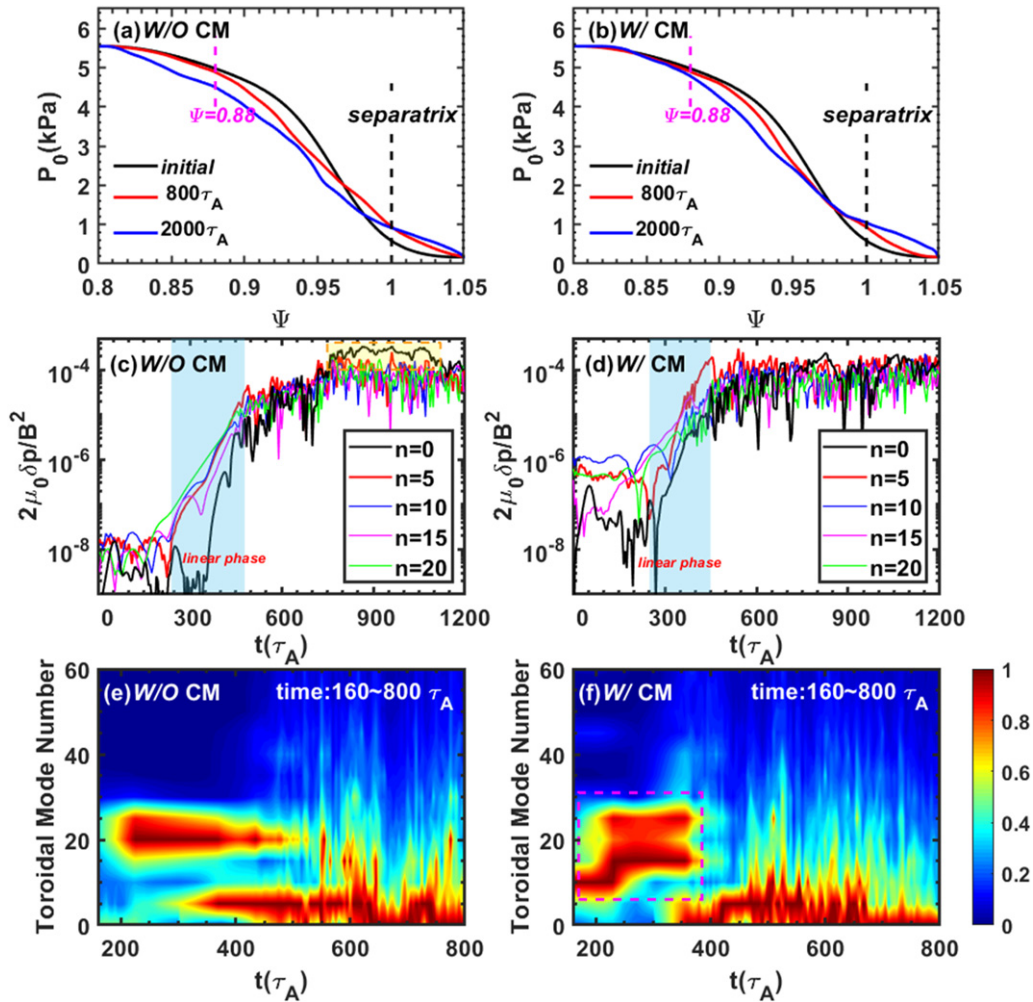


Figure 13. (a) Evolution of the radial pressure profile on the outer mid-plane at different time slices without the CM; (c) the time evolution of the different toroidal modes without CM; (e) the evolution of normalized mode spectrum without CM in the time $160\text{--}800\tau_A$; the data in (c) and (e) are taken from the same location. The (b), (d) and (f) are the same plot for the case with CM. The (e) and (f) have the same color bar.

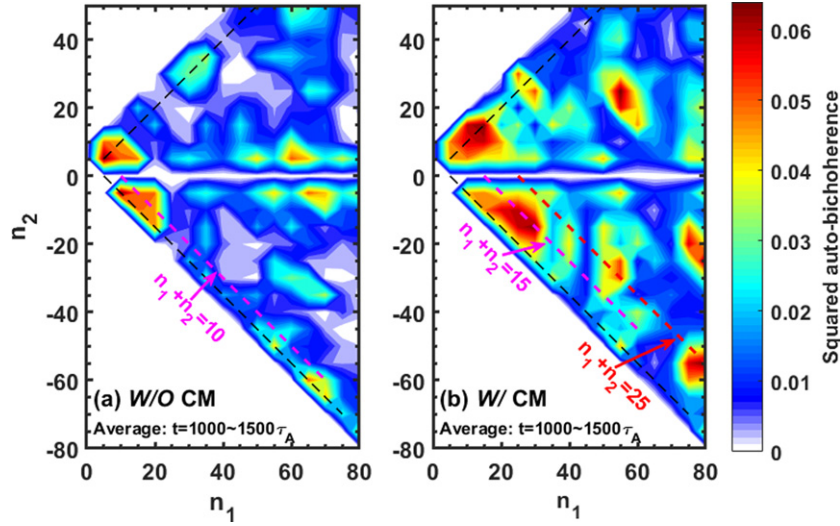


Figure 14. The squared auto-bicoherence $\hat{b}_{p_n p_n p_n}^2(n_1, n_2)$ of nonlinear P–B modes for different cases. (a) The case without CM; and (b) the case with CM. The (a) and (b) have the same color bar.

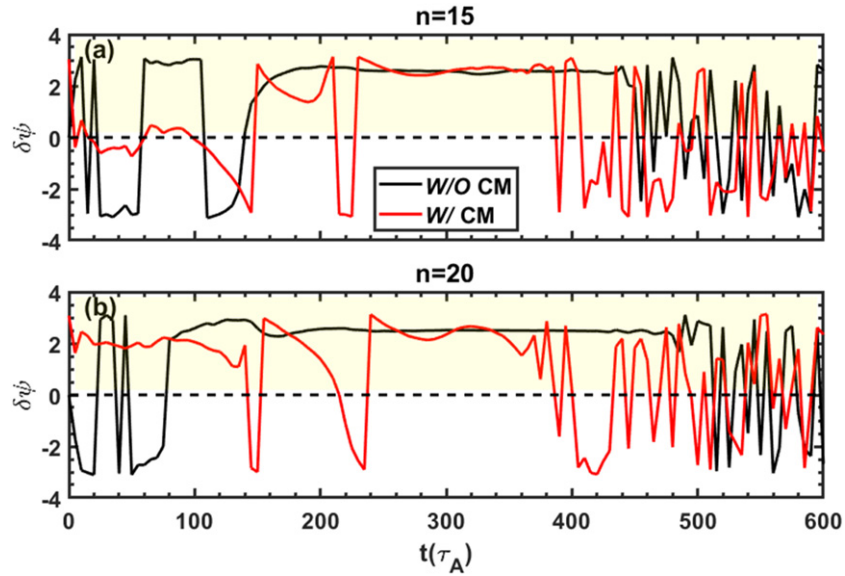


Figure 15. Evolution of relative phase $\delta\varphi$ between perturbed pressure (\tilde{p}_n) and perturbed potential ($\tilde{\phi}_n$). (a) $n = 15$ for with and without the CM; (b) the same plot for $n = 20$. The dashed black line corresponds to $\delta\varphi = 0$.

w/ CM [44, 55, 56]. The case w/o CM tends to be ‘single-mode’, but that w/ CM tends to be ‘multiple-mode’ coupling. The multiple-mode coupling can reduce the energy loss effectively.

4.3. The relative phase and phase coherence time (PCT)

Typically, the growth of the perturbation amplitude depends on both the linear drive and the nonlinear wave–wave interactions. For the linear drive, both a sufficient growth rate and an effective growth time are required. It is already clear that the growth rate $\gamma(n)$ has been changed by CM from the evolution of pressure fluctuations in figure 13. Now, the effective growth time is analyzed. In our simulations, the linear

dominant mode is near the medium n -mode, and the instability is mainly driven by the ballooning mode. Therefore, the dependence of the perturbed energy on the curvature term is written as [44]

$$\frac{\partial \tilde{V}_{E \times B, n}^2}{\partial t} \propto -2\Re(\text{in} \hat{\phi}_n^* \hat{P}_n b_0 \times \kappa \cdot \nabla \zeta) \propto \sin \delta\varphi. \quad (15)$$

Here, $\delta\varphi$ represents the relative phase between \hat{P}_n and $\hat{\phi}_n$, which is calculated by

$$\delta\varphi(n, \psi, \theta, t) = \arg \left[\hat{P}_n(\psi, \theta, t) / \hat{\phi}_n(\psi, \theta, t) \right], \delta\varphi \in (-\pi, \pi]. \quad (16)$$

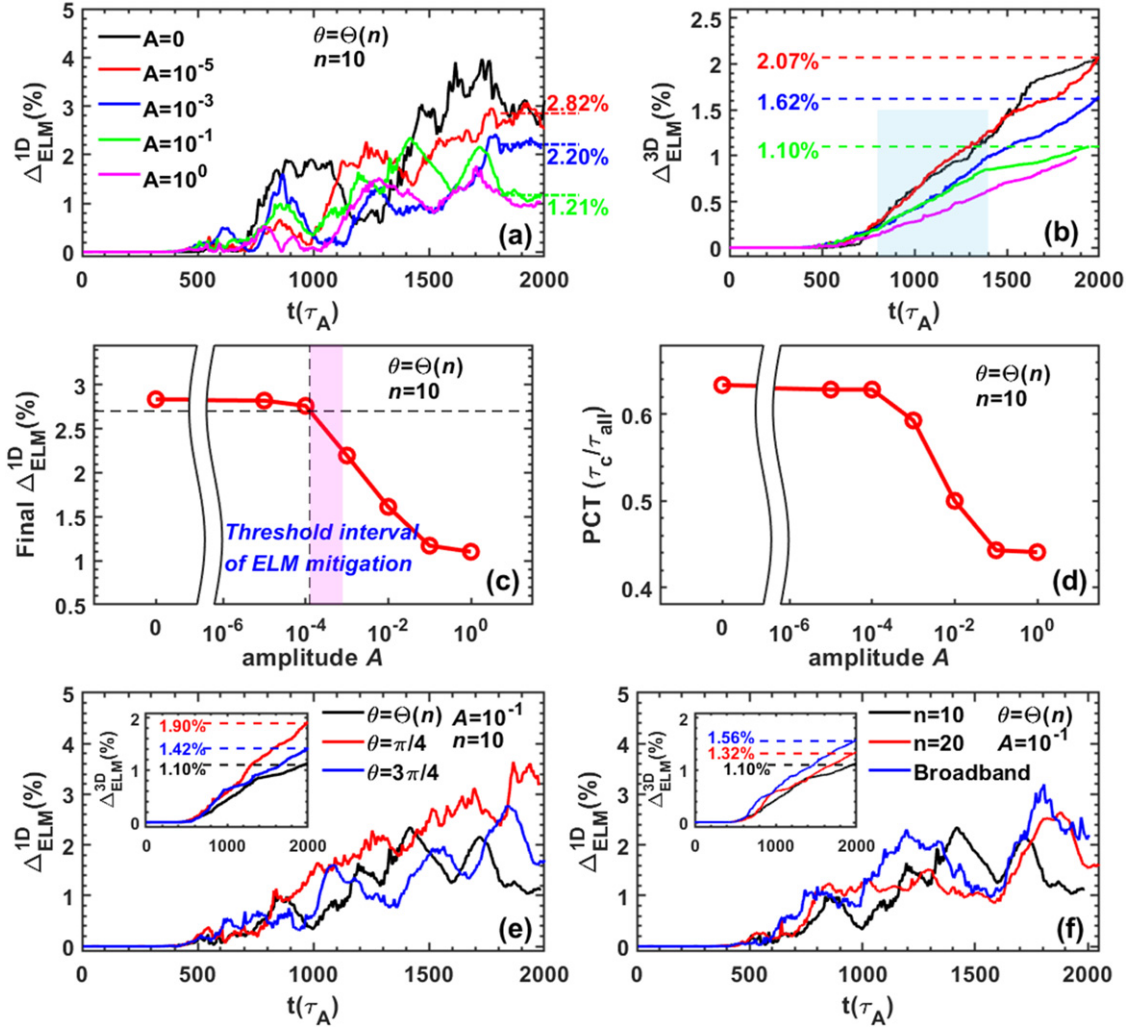


Figure 16. The time evolution of ELM size for different CM cases. (a) The $\Delta_{\text{ELM}}^{1\text{D}}$ of different turbulent amplitudes with $\theta = \Theta(n)$ and dominant mode $n = 10$: $A = 0$ (black curve), $A = 10^{-5}$ (red curve), $A = 10^{-3}$ (blue curve), $A = 10^{-1}$ (green curve) and $A = 10^0$ (magenta curve); (b) the $\Delta_{\text{ELM}}^{3\text{D}}$ of the same cases in panel (a); (c) the final ELM size ($\Delta_{\text{ELM}}^{1\text{D}}$) vs the amplitude A spectrum, and (d) the PCT vs the amplitude A of the dominated mode (the total time $\tau_{\text{all}} = 2000\tau_A$). (e) The ELM size of different turbulent phases with $A = 10^{-1}$ and $n = 10$: $\theta = \pi/4$ (red curve), $\theta = 3\pi/4$ (blue curve) and $\theta = \Theta(n)$ (black curve); (f) the ELM size of different toroidal mode number spectrums with $A = 10^{-1}$ and $\theta = \Theta(n)$: the dominant mode $n = 10$ (black curve), $n = 20$ (red curve) and broadband turbulence (blue curve). The inset panels in (e) and (f) are $\Delta_{\text{ELM}}^{3\text{D}}$ for the same cases.

The \hat{P}_n and $\hat{\phi}_n$ are the n th toroidal Fourier quantities of the pressure and potential fluctuations, respectively. The relative phase $\delta\varphi$ can determine whether the ballooning modes can obtain the free energy driven by the pressure gradient. The mode amplitudes are increasing only when $0 < \delta\varphi < \pi$ and damping when $-\pi < \delta\varphi < 0$. The time duration of mode growth is called phase coherence time (PCT) $\tau_c(n)$, and the net increase of fluctuations during the linear phase is set to $\gamma(n) \cdot \tau_c(n)$ [44, 56].

In this paper, the dominant mode during the linear growth phase is near $n = 20$ in the case w/o the CM as shown in figure 13(e). Consequently, the relative phase ($\delta\varphi$) of the modes $n = 15, 20$ are given in figure 15. After adding the \tilde{p}_{CM} terms, $\delta\varphi$ is oscillated more frequently and the time for $0 < \delta\varphi < \pi$ is less than the case w/o CM during $200\text{--}450\tau_A$. Therefore, the PCT (τ_c) w/ CM becomes shorter, which results

in the smaller fluctuation amplitudes. This indicates that the fluctuation extracts less free energy from the pressure gradient and the ELM is mitigated effectively. What's more, in the non-linear phase (about $500\text{--}600\tau_A$) of both cases, $\delta\varphi$ oscillates rapidly between positive and negative values caused by the wave-wave interactions. Thus, there is no significant growth of the mode amplitude in the nonlinear phase.

5. Factor analysis of the CM

Based on the previous analysis, it is clear that the CM plays an important role in the ELM mitigation. In equation (12), \tilde{p}_{CM} has three decisive parameters: amplitude A , phase θ , and spectrum $\bar{P}_{kz}(n)$. In order to find the optimal amount of perturbation to mitigate the ELM, the three parameters are scanned. We have divided the simulated cases into three groups: (1) set

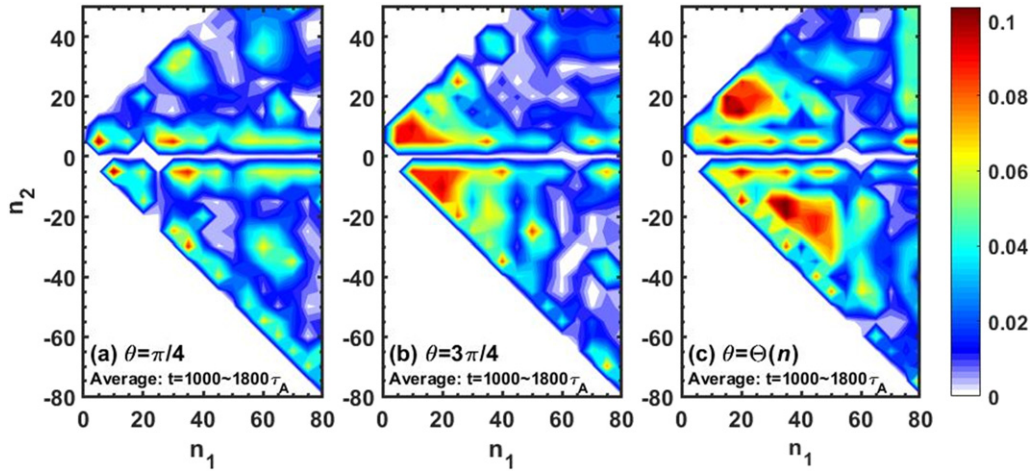


Figure 17. 2D auto-bicoherence $\hat{b}_{p_n p_n p_n}^2(n_1, n_2)$ for different turbulent phases of CM: (a) $\theta = \pi/4$; (b) $\theta = 3\pi/4$; and (c) $\theta = \Theta(n)$. The amplitude $A = 10^{-1}$ and the dominant mode $n = 10$. All the subgraphs have the same color bar.

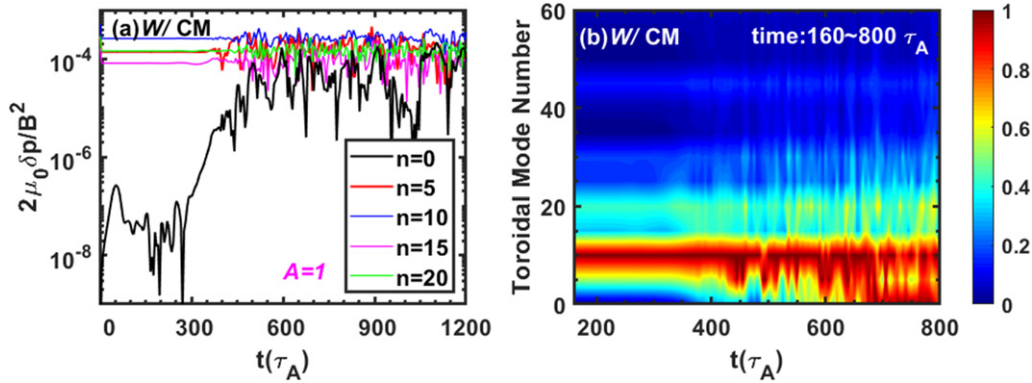


Figure 18. The case with the CM for $\theta = \Theta(n)$, $A = 10^0$ and the dominant mode $n = 10$. (a) The evolution of different toroidal modes; (b) the evolution of the mode spectrum.

phase $\theta = \Theta(n)$ and $\bar{P}_{kz}(n)$ to the spectra of dominant mode $n = 10$ as shown in figure 9, and scan the amplitude: $A = 0, 10^{-5}, 10^{-3}, 10^{-1}$ and 10^0 ; (2) set $A = 10^{-1}$ and $\bar{P}_{kz}(n)$ to the same as set in (1), then scan the phase: for different n modes, $\theta = \pi/4, \theta = 3\pi/4$, and $\theta = \Theta(n)$; (3) set $A = 10^{-1}$ and $\theta = \Theta(n)$, the spectra $\bar{P}_{kz}(n)$ are scanned: the dominant mode $n = 10, n = 20$ and the broadband turbulence, just as shown in figure 9(a). The results of the simulations are shown in figure 16.

Figure 16 gives the time evolution of the ELM size for different parameters of \tilde{p}_{CM} . In the figure 16(a), the results of different amplitudes are shown. The red solid curve is the ELM size of the amplitude $A = 10^{-5}$ case, the blue, green and magenta curves represent the $A = 10^{-3}, A = 10^{-1}$ and $A = 1$ cases, respectively. The black solid curve is the case w/o CM in section 2.3, which is only used here for comparison. It indicates that the ELM size has a strong correlation with the amplitude A . By comparison, a significant difference in the changing rate of the Δ^{3D}_{ELM} appears during $800-1400\tau_A$ in the figure 16(b), and it can be divided into three cases: (1)

the amplitude is very small ($A = 0$ and $A = 10^{-5}$), the changing rate is maximum; (2) using the finite-amplitude ($A = 10^{-3}$ and $A = 10^{-1}$), the changing rate is medium; and (3) when $\delta p \sim P_0$, i.e. $A = 1$, the changing rate is minimum. Figure 16(c) gives the dependence of the final ELM size on the amplitude A , and there is a threshold of the ELM mitigation in the magenta region, which is consistent with the experimental statistical results shown in figure 2. The ELM can be mitigated when the amplitude is large enough. The larger the CM amplitude is, the smaller the ELM size trends to be. The relation between PCT and amplitude A in figure 16(d) is also consistent with the ELM-size reduction in large CM amplitude, which indicates that the large amplitude can reduce the growth time of the perturbation and the ELM energy loss. Figure 16(e) shows the ELM size for different phase cases. All of the three cases start to enter the initial ELM crash phase at about $t = 500\tau_A$. The ELM size of the fixed phase $\theta = \pi/4$ case is about 3.40%, the $\theta = 3\pi/4$ case is 1.68%, and the $\theta = \Theta(n)$ case is 1.20%. We can see that the different phases also have an important effect on the energy loss, and the $\theta = \pi/4$ case is about three times as large as the $\theta = \Theta(n)$ case. Figure 16(f) reveals the impact

of different toroidal mode spectrums, and the ELM sizes of the three cases are eventually different. Although the different spectrums $\bar{P}_{kz}(n)$ can cause some influence, its effect is smaller compared to the amplitude A and phase θ .

In conclusion, it is clear from all the cases that the amplitude A plays a key role and has a threshold value beyond which the ELM size is reduced. This demonstrates that ELMs can be mitigated when the edge perturbation is enhanced. What's more, the effect of the phase θ is probably very important in our simulation when the amplitude A is determined, while the spectrum $\bar{P}_{kz}(n)$ also has an effect and should not be neglected.

In the previous analysis, the influence of the phases is very important with a determined amplitude, probably because the phase alteration affects the wave-wave interactions and changes the PCT. Thus, the nonlinear mode coupling is analyzed based on the cases in figure 16(e). The 2D auto-coherence of different CM phases at the time average of $t = 1000\text{--}1800\tau_A$ are shown in figure 17: the $\theta = \pi/4$ case is exhibited in the panel (a), $\theta = 3\pi/4$ and $\theta = \Theta(n)$ cases are the panel (b) and (c). Compared to $\theta = \pi/4$, there are more medium and high n mode coupling in the $\theta = 3\pi/4$ or $\theta = \Theta(n)$ case, which indicates that the nonlinear wave-wave interactions become stronger and the PCT gets decreased dramatically. The more mode coupling leads to the lack of dominant filamentary structures and smaller ELM energy loss [19, 44, 55, 57, 58]. In addition, the higher n modes appear in the $\theta = \Theta(n)$ case by comparing with $\theta = 3\pi/4$ case. Finally, it is found that the ELM size with $\theta = \pi/4$ is larger than $\theta = 3\pi/4$, and the $\theta = 3\pi/4$ case is larger than $\theta = \Theta(n)$, i.e. $\Delta_{\text{ELM}}^{\theta=\pi/4} > \Delta_{\text{ELM}}^{\theta=3\pi/4} > \Delta_{\text{ELM}}^{\theta=\Theta(n)}$. The result is reasonable that the ELM size of $\theta = \Theta(n)$ is smaller. The random-like phase $\Theta(n)$ comes from the simulation in section 2.3, in which the CM is formed by the profile auto-evolution. Therefore, the CM perturbation (\tilde{p}_{CM}) of $\theta = \Theta(n)$ is very close to the eigenmode. The $\theta = \Theta(n)$ case is nearly in-phase with the pressure perturbation, which is easy to get coupled, but that of $\theta = \pi/4$ or $3\pi/4$ case is likely out-of-phase, which is hard to be coupled. Only when the CM phase and pressure phase are similarly in-phase, the nonlinear interactions can be enhanced and the ELM can be mitigated effectively.

As for the extreme case of CM amplitude $A = 1$, it is almost impossible in reality. However, because the CM amplitude is too large and almost at the same level as pressure P_0 , there may be some interesting physical phenomena. Thus, it is interesting to analyze the process of ELM crash with $A = 1$. The evolution of the pressure perturbation with the CM for phase $\theta = \Theta(n)$ and amplitude $A = 1$ is shown in the figure 18. Figure 18(a) is the time evolution of the fluctuation for different toroidal modes, and figure 18(b) is the mode spectrum evolution. It can be seen that all modes are kept at the level of the CM in the whole simulation, which means the nonlinear dynamics are always dominated by the large CM perturbation, which cannot happen in the $A < 1$ cases. Only the $n = 0$ mode grows up slowly because of the lack of zonal component in the constructed CM. When the amplitude of the $n = 0$ mode increases large enough, the profile collapses and it enters the nonlinear phase. This suggests that the zonal part of the perturbation plays a crucial role in the ELM crash [56]. The ELM

can only be triggered when the amplitude of $n = 0$ mode is large enough. The presence of the CM leads to less free energy redistributed to the $n = 0$ mode, and eventually the ELM is effectively mitigated.

6. Summary

In EAST, the phenomenon that the ELMs are mitigated with the enhanced CM has been observed. Through statistical analysis, a threshold of the CM intensity is found for ELM mitigation, and only above the threshold value can the ELM be effectively mitigated. However, the results of ELITE analysis show that the pedestal is located outside the P-B boundary when the no ELM and the enhanced CM co-exist. The results only considering the pedestal profiles are not consistent with the experiment. Therefore, the effects of the enhanced CM are considered to explain the mitigation of ELM.

The impact of the CM on ELMs are investigated using the extended three-field two-fluid model in BOUT++ framework. For simplicity, we assume that the CM is mainly the perturbations of pressure due to the density gradient, which is essentially consistent with the most of EAST experiments. To incorporate the effect of the CM, the quantity \tilde{p}_{CM} is introduced in the model, as the additional convective and driving terms in the pressure and vorticity evolution equations in equations (7)–(9). In the experiment, the CM is a flute-like mode (i.e. $k_{\parallel} \sim 0$), and the poloidal distribution of the density fluctuation demonstrates a ballooning-like structure [16]. Based on these characteristics, the CM distribution \tilde{p}_{CM} can be described by equation (12) in the simulation.

The interactions between the ELM and CM are studied in the paper. The simulations show that the CM is able to reduce the ELM size by $\sim 44.5\%$, and the amplitude of pressure perturbation is dropped by about half in the nonlinear phase. What's more, the radial mode expansion is limited by the CM, and the mode spectrum is explicitly shifted in the linear phase. The physics mechanism of the ELM mitigation by CM can be explained by the nonlinear wave-wave interactions. Through the bi-spectral and the relative phase analysis, the nonlinear interactions and mode coupling are stronger with the CM, and the PCT becomes smaller. This indicates that more modes can compete with the eigenmode for free energy and the turbulence behaviors are changed, which leads to the obvious mitigation of the ELM. In addition, the parameters (A , θ and \bar{P}_{kz}) of the CM are scanned, and it is found that: (1) the impact of the amplitude A is probably the most important, and A has a clear threshold value to mitigate the ELM; (2) with a determined A , the phase θ plays a role, but the spectra $\bar{P}_{kz}(n)$ also has some influences and cannot be ignored. The simulation systematically investigates the interactions between ELM and CM, which can provide support for the development of ELM control technology.


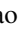
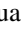

Notice that this work mainly focuses on the ELM mitigation induced by the enhanced CM. The interactions between ELMs and CMs are studied. However, in some experimental cases, the ELM is fully suppressed. There must be other

factors missed in the ELM suppression, such as auxiliary heating, impurity and power deposition effects, which will be investigated step by step in the future.

Acknowledgments

The authors wish to acknowledge Dr B. Chen, Dr Z.Y. Li and Dr Y.P. Zou for useful discussions. This work is supported by the National Key R&D Program of China under Nos. 2017YFE0301101 and 2019YFE03030004, the National Natural Science Foundation of China under Grant Nos. 12175275, 11975232 and 11675217, the Comprehensive Research Facility for Fusion Technology Program of China under Contract No. 2018-000052-73-01-001228, and the Collaborative Innovation Program of Hefei Science Center, CAS, 2021HSC-CIP018. This work is also sponsored in part by Youth Innovation Promotion Association Chinese Academy of Sciences (Y2021114). Numerical computations were performed on the ShenMa High Performance Computing Cluster in Institute of Plasma Physics, Chinese Academy of Sciences, and the CFETR Integration Design Platform (CIDP) in the Supercomputing Center of University of Science and Technology of China.

ORCID iDs

Y.L. Li  <https://orcid.org/0000-0002-3607-7654>
 S.F. Mao  <https://orcid.org/0000-0002-2370-1585>
 Y.Q. Huang  <https://orcid.org/0000-0002-3133-9854>
 M.Y. Ye  <https://orcid.org/0000-0002-9055-1476>

References

- [1] Wagner F. et al 1982 *Phys. Rev. Lett.* **49** 1408–12
- [2] Keilhacker M. et al 1984 *Plasma Phys. Control. Fusion* **26** 49
- [3] Leonard A.W. 2014 *Phys. Plasmas* **21** 090501
- [4] Huijsmans G.T.A., Chang C.S., Ferraro N., Sugiyama L., Waelbroeck F., Xu X.Q., Loarte A. and Futatani S. 2015 *Phys. Plasmas* **22** 021805
- [5] Snyder P.B. et al 2009 *Nucl. Fusion* **49** 085035
- [6] Evans T.E. et al 2004 *Phys. Rev. Lett.* **92** 235003
- [7] Sun Y. et al 2016 *Phys. Rev. Lett.* **117** 115001
- [8] Liang Y. et al 2013 *Phys. Rev. Lett.* **110** 235002
- [9] Xiao G.L. et al 2017 *Phys. Plasmas* **24** 122507
- [10] Xiao G.L. et al 2019 *Nucl. Fusion* **59** 126033
- [11] Baylor L.R. et al 2013 *Phys. Rev. Lett.* **110** 245001
- [12] Hu J.S. et al 2015 *Phys. Rev. Lett.* **114** 055001
- [13] Xia T.Y., Gui B., Huang Y.Q., Wu Y.B. and Xiao X.T. 2019 *Nucl. Fusion* **59** 076043
- [14] Lan H. et al 2019 *Phys. Plasmas* **26** 122505
- [15] Gao X. et al 2015 *Nucl. Fusion* **55** 083015
- [16] Zhang T. et al 2017 *Plasma Phys. Control. Fusion* **59** 065012
- [17] Wang H.Q. et al 2014 *Phys. Rev. Lett.* **112** 185004
- [18] Wang H.Q. et al 2014 *Phys. Plasmas* **21** 092511
- [19] Diallo A., Dominski J., Barada K., Knolker M., Kramer G.J. and McKee G. 2018 *Phys. Rev. Lett.* **121** 235001
- [20] Chen R. et al 2018 *Nucl. Fusion* **58** 112004
- [21] Mazurenko A., Porkolab M., Mossessian D., Snipes J.A., Xu X.Q. and Nevins W.M. 2002 *Phys. Rev. Lett.* **89** 225004
- [22] LaBombard B. and Lyons L. 2007 *Rev. Sci. Instrum.* **78** 073501
- [23] Yan Z. et al 2011 *Phys. Rev. Lett.* **107** 055004
- [24] Garofalo A.M. et al 2015 *Phys. Plasmas* **22** 056116
- [25] Suttrop W. et al 2005 *Nucl. Fusion* **45** 721–30
- [26] White A.E., Phillips P., Whyte D.G., Hubbard A.E., Sung C., Hughes J.W., Dominguez A., Terry J. and Cziegler I. 2011 *Nucl. Fusion* **51** 113005
- [27] Manz P. et al 2017 *Nucl. Fusion* **57** 086022
- [28] Vanovac B. et al 2018 *Nucl. Fusion* **58** 112011
- [29] Xu X.Q., Dudson B., Snyder P.B., Umansky M.V. and Wilson H. 2010 *Phys. Rev. Lett.* **105** 175005
- [30] Xu X.Q., Dudson B.D., Snyder P.B., Umansky M.V., Wilson H.R. and Casper T. 2011 *Nucl. Fusion* **51** 103040
- [31] Xia T.Y. and Xu X.Q. 2015 *Nucl. Fusion* **55** 113030
- [32] Dong L., Chen S., Mou M. and Tang C. 2020 *Plasma Sci. Technol.* **22** 115101
- [33] Li M., Sun J., Wang Y. and Xia T. 2021 *Nucl. Mater. Energy* **26** 100888
- [34] Ji J. et al 2021 *Plasma Sci. Technol.* **23** 095106
- [35] Feng X. et al 2019 *Rev. Sci. Instrum.* **90** 024704
- [36] Hu J.Q. et al 2017 *Rev. Sci. Instrum.* **88** 073504
- [37] Lang P.T., Alper B., Buttery R., Gal K., Hobirk J., Neuhauser J. and Stamp M. (JET-EFDA contributors) 2007 *Nucl. Fusion* **47** 754–61
- [38] Chankin A.V., Asakura N., Fukuda T., Isayama A., Kamada Y., Miura Y., Oyama N., Takeji S. and Takenaga H. 2002 *Nucl. Fusion* **42** 733–42
- [39] Kass T., Günter S., Maraschek M., Suttrop W. and Zohm H. (ASDEX Upgrade Team) 1998 *Nucl. Fusion* **38** 111–6
- [40] Wu N. et al 2021 *Plasma Phys. Control. Fusion* **63** 075002
- [41] Snyder P.B. et al 2002 *Phys. Plasmas* **9** 2037–43
- [42] Lao L.L., John H.E.S., Peng Q., Ferron J.R., Strait E.J., Taylor T.S., Meyer W.H., Zhang C. and You K.I. 2005 *Fusion Sci. Technol.* **48** 968–77
- [43] Dudson B.D., Umansky M.V., Xu X.Q., Snyder P.B. and Wilson H.R. 2009 *Comput. Phys. Commun.* **180** 1467–80
- [44] Xi P.W., Xu X.Q. and Diamond P.H. 2014 *Phys. Rev. Lett.* **112** 085001
- [45] Xi P.W., Xu X.Q., Wang X.G. and Xia T.Y. 2012 *Phys. Plasmas* **19** 092503
- [46] Zhang X. et al 2020 *Plasma Phys. Control. Fusion* **62** 095007
- [47] Zhou Z. et al 2021 *Plasma Sci. Technol.* **23** 075101
- [48] Xia T.Y., Xu X.Q. and Xi P.W. 2013 *Nucl. Fusion* **53** 073009
- [49] Chen B. et al 2018 *Phys. Plasmas* **25** 055905
- [50] Tang T.F., Shi H., Wang Z.H., Zhong W.L., Xia T.Y., Xu X.Q., Sun J.Z. and Wang D.Z. 2018 *Phys. Plasmas* **25** 122510
- [51] Gürçan Ö.D., Garbet X., Hennequin P., Diamond P.H., Casati A. and Falchetto G.L. 2009 *Phys. Rev. Lett.* **102** 255002
- [52] Kim Y.C. and Powers E.J. 1978 *Phys. Fluids* **21** 1452
- [53] Kim Y.C. and Powers E.J. 1979 *IEEE Trans. Plasma Sci.* **7** 120–31
- [54] Lan T. et al 2008 *Plasma Phys. Control. Fusion* **50** 045002
- [55] Xu X.Q., Xia T.Y., Yan N., Liu Z.X., Kong D.F., Diallo A., Groebner R.J., Hubbard A.E. and Hughes J.W. 2016 *Phys. Plasmas* **23** 055901
- [56] Huang Y.Q. et al 2020 *Nucl. Fusion* **60** 026014
- [57] Chen J.G., Xu X.Q., Ma C.H., Xi P.W., Kong D.F. and Lei Y.A. 2017 *Phys. Plasmas* **24** 050704
- [58] Ishizawa A. and Nakajima N. 2007 *Nucl. Fusion* **47** 1540–51